

Chain of Flow: A Foundational Generative Framework for ECG-to-4D Cardiac Digital Twins

Haofan Wu, Nay Aung, Theodoros N. Arvanitis, Joao A. C. Lima, Steffen E. Petersen, Le Zhang

Abstract—A clinically actionable Cardiac Digital Twin (CDT) should reconstruct individualised cardiac anatomy and physiology, update its internal state from multimodal signals, and enable a broad range of downstream simulations beyond isolated tasks. However, existing CDT frameworks remain limited to task-specific predictors rather than building a patient-specific, manipulable virtual heart. In this work, we introduce Chain of Flow (COF), a foundational ECG-driven generative framework that reconstructs full 4D cardiac structure and motion from a single cardiac cycle. The method integrates cine-CMR and 12-lead ECG during training to learn a unified representation of cardiac geometry, electrophysiology, and motion dynamics. We evaluate Chain of Flow on diverse cohorts and demonstrate accurate recovery of cardiac anatomy, chamber-wise function, and dynamic motion patterns. The reconstructed 4D hearts further support downstream CDT tasks such as volumetry, regional function analysis, and virtual cine synthesis. By enabling full 4D organ reconstruction directly from ECG, COF transforms cardiac digital twins from narrow predictive models into fully generative, patient-specific virtual hearts. *Code will be released after review.*

Index Terms—Cardiac digital twin, electrophysiology, 4D cardiac reconstruction, patient-specific modelling, multi-modal learning.

I. INTRODUCTION

CARDIOVASCULAR diseases remain the leading cause of morbidity and mortality worldwide [1]. Accurate evaluation of cardiac anatomy and function is essential for diagnosis, risk stratification, and treatment planning [2], [3]. High-precision quantification of chamber volumes, myocardial deformation, and regional function provides clinicians with valuable information for supporting clinical decision-making [4]. Cardiac Digital Twin technology has emerged as a promising framework for building patient-specific virtual hearts that can represent anatomy, physiology, and dynamic motion within a unified computational model [5]. A clinically actionable

CDT could, in principle, integrate multimodal data, provide real-time visualisations of cardiac behaviour, and support a wide range of downstream simulations—from volumetric assessment to functional analysis and disease progression modelling [6]. Such capabilities would enable scalable, individualised evaluation of cardiac function far beyond the constraints of conventional imaging pipelines [7].

In practice, however, creating a CDT that is both anatomically faithful and clinically accessible requires a structural backbone that provides segmentation-meaningful 3D geometry and physiologically interpretable motion. CMR is currently the only modality capable of delivering this level of detail, making it the natural foundation for constructing high-fidelity CDTs [8]. Yet the reliance on CMR severely limits scalability: the modality is expensive, scanner-dependent, and difficult to acquire repeatedly, and its availability varies greatly across healthcare systems [9]. These constraints hinder the deployment of CMR-based CDTs in routine clinical workflows.

In contrast, the electrocardiogram (ECG) is inexpensive, ubiquitous, and continuously measurable, offering an attractive alternative input for building scalable and longitudinally updated CDTs [10]. However, ECG signals capture only the electrical projection of cardiac activity and do not contain explicit anatomical information, making the inverse mapping from ECG to full cardiac geometry and motion extremely challenging [11]. Bridging ECG and CMR in a unified generative framework would enable anatomically meaningful 4D cardiac reconstruction directly from ECG while preserving the segmentation standards and physiological interpretability required for CDT applications [12].

In this work, we propose COF, a foundational ECG-driven generative framework designed to overcome these limitations. COF reconstructs full 4D cardiac structure and motion directly from a single cardiac cycle of 12-lead ECG. During training, COF integrates cine-CMR and ECG to learn a unified representation of cardiac geometry, electrophysiology, and dynamic motion patterns. Unlike traditional task-restricted CDT models, COF performs full organ-level generation, enabling the synthesis of patient-specific virtual hearts with an anchor at inference. We evaluate COF across diverse patient cohorts and demonstrate accurate recovery of cardiac anatomy, chamber-wise function, and physiologically consistent 4D motion. The reconstructed virtual hearts further support key CDT applications, including volumetry, regional function analysis, motion tracking, and virtual cine synthesis. An overview of the framework is shown in Fig. 1. The main contributions of

Haofan Wu, Theodoros N. Arvanitis and Le Zhang are with the School of Engineering, College of Engineering and Physical Sciences, University of Birmingham, Birmingham, United Kingdom. Le Zhang is also with William Harvey Research Institute, NIHR Barts Biomedical Research Centre, Queen Mary University London, London, United Kingdom.

Nay Aung, Steffen E. Petersen are with William Harvey Research Institute, NIHR Barts Biomedical Research Centre, Queen Mary University London, London, United Kingdom, and Barts Heart Centre, St Bartholomew's Hospital, Barts Health NHS Trust, West Smithfield, London, United Kingdom.

Joao A. C. Lima is with Division of Cardiology, Johns Hopkins University School of Medicine, Baltimore, Maryland, United States.

Corresponding Author: Le Zhang (l.zhang.16@bham.ac.uk)

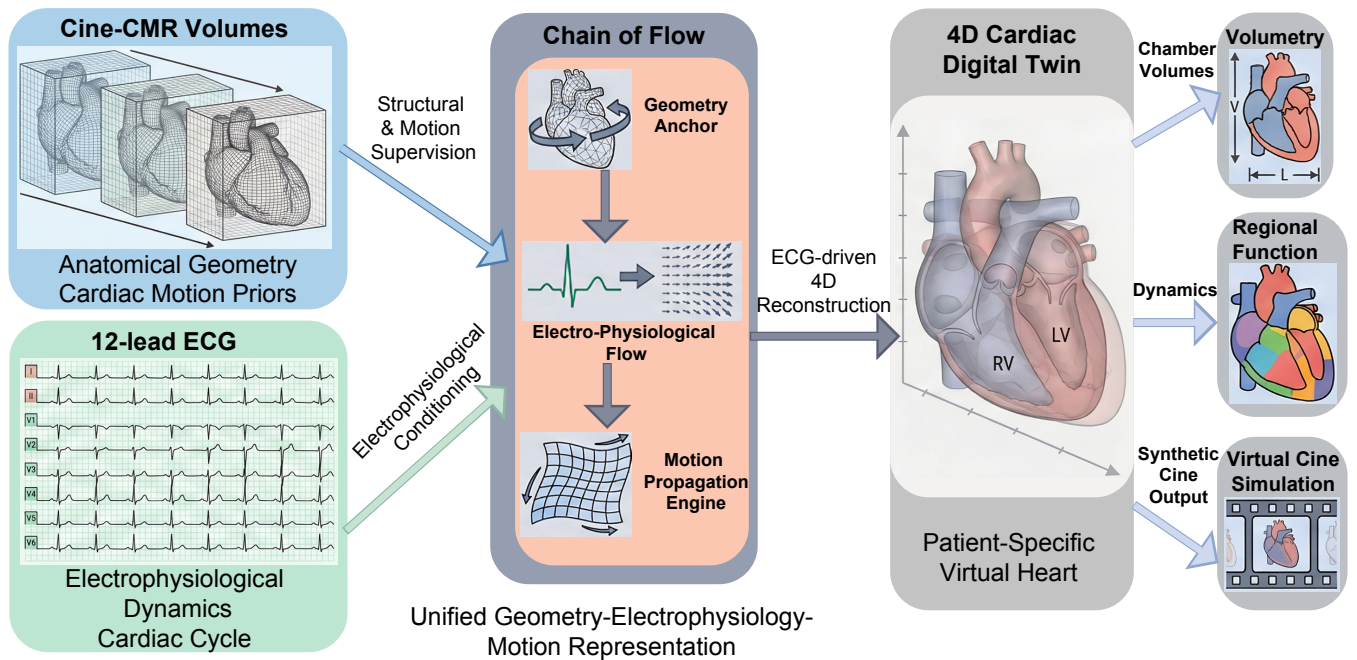


Fig. 1. Overview of the COF for ECG-driven cardiac digital twin generation. The framework integrates CMR volumes and 12-lead ECG during training to learn a unified representation of cardiac anatomy, electrophysiology, and motion dynamics. Cine-CMR provides anatomical geometry and motion supervision, while ECG supplies subject-specific electrophysiological dynamics over a single cardiac cycle. These multimodal signals are fused within the proposed Chain of Flow, which couples geometry encoding, electro-physiological flow, and motion propagation to form a unified ECG-driven generative representation. At inference, the learned model reconstructs a patient-specific 4D cardiac digital twin directly from ECG, yielding individualised cardiac anatomy and motion. The resulting digital heart supports downstream CDT applications, including chamber volumetry, regional functional analysis, and virtual cine simulation.

this work are as follows:

- We propose **COF**, an ECG-conditioned generative framework that reconstructs full 4D cine CMR volumes from a single cardiac cycle, producing anatomically coherent and temporally continuous sequences.
- We introduce a **registration-derived motion supervision and flow matching mechanism** that injects ECG dynamics into a topology-preserving motion field while separating static anatomy from temporal dynamics.
- We verify generalisation through **slice-wise and resolution-wise evaluations**, and demonstrate robust performance across **multiple ECG-derived disease categories**.
- We demonstrate that COF is **digital-twin ready** by validating functional cardiac indices derived from the generated 4D cine volumes.

II. RELATED WORK

A. Cardiac Digital Twin

CDTs aim to create virtual patient-specific hearts capable of representing anatomy, physiology, and dynamic function within a unified computational platform [6]. In principle, a CDT should provide anatomically resolved 3D geometry, physiologically meaningful motion, and the ability to support downstream analyses such as volumetry [13], regional function assessment [14], and virtual simulation of disease progression or interventions [15]. However, existing CDT frameworks fall short of this vision [6]. Most approaches operate as parameter-level predictors, estimating a limited

set of functional indices—such as ejection fraction [16], scar burden [17], myocardial activation timing [18], pressure–volume relationships [19], or simplified electrophysiological states [20]—from imaging or electrophysiological inputs. These models do not reconstruct the full cardiac anatomy, nor do they provide a manipulable virtual organ that preserves segmentation-meaningful structure and 4D motion. Other CDT-related methods combine imaging, electrophysiology, and simulated biophysical models to estimate localised cardiac properties [18], [21]. While these frameworks improve physiological interpretability, they still produce low-dimensional summaries rather than a full 4D representation of the heart [19]. More importantly, they rely on predefined parameterisations or simplified forward models, which limit flexibility and prevent them from capturing patient-specific anatomical variability and motion patterns [17]. Consequently, these systems cannot generalise to diverse patient populations or support tasks beyond the specific quantities they were trained to predict [16]. These limitations motivate a generative framework that reconstructs full cardiac anatomy and motion from widely available physiological signals [5], [22].

B. Generative Models for Cardiac Structure and Motion

Generative modelling has recently gained traction in cardiac imaging for reconstructing anatomical structure, synthesising cine sequences, and improving image quality [23], [24]. Variational autoencoders, diffusion models, and flow-based generative frameworks have been applied to tasks such as cine reconstruction, motion estimation, and cross-modality synthe-

sis [25], [26]. These methods learn latent representations of cardiac geometry and temporal deformation, offering improved robustness to noise and enabling realistic generation of 3D or 4D cardiac volumes [25], [26]. However, existing generative frameworks are fundamentally conditioned on explicit imaging inputs—such as cine CMR [26]—which provide dense spatial information during inference. Although recent studies have explored cross-modal synthesis between imaging modalities, these approaches still assume shared spatial structure or paired volumetric data and rely on visually aligned supervision. Such assumptions break down for ECG signals, which lack explicit anatomical correspondence. More critically, current cross-modal generative models prioritise perceptual realism over anatomical fidelity [27]. When applied to cardiac anatomy, this often leads to blurred boundaries, distorted chamber geometry, and inconsistent myocardial thickness—errors that are unacceptable for organ-level CDTs [28] requiring segmentation-meaningful structure and temporally coherent motion [29]. Without explicit anatomical or physiological constraints, these models also fail to preserve consistent deformation patterns across the cardiac cycle [30]. This motivates an ECG-conditioned generative framework that preserves anatomical fidelity and coherent motion, while generated cine CMR can support downstream pretraining [31].

C. ECG-Based Cardiac Modelling

The 12-lead electrocardiogram is one of the most accessible and widely used non-invasive tools for cardiac assessment [32]. Prior studies have leveraged ECG to estimate global functional parameters such as heart rate variability, conduction delays, and ventricular hypertrophy indices [33], or to classify arrhythmias and ischaemic abnormalities [34], [35]. In the context of structural heart disease, several studies have leveraged ECG signals to infer myocardial infarction (MI) characteristics—such as infarct location [36], transmural extent [37], or electrical activation abnormalities—from QRS or ST-T patterns [38]. While these approaches demonstrate the diagnostic value of ECG, their outputs are inherently low-dimensional and do not capture the full geometric or dynamic complexity of the heart. Beyond functional estimation, ECG has also been used to address the inverse electrophysiology problem, aiming to recover myocardial electrical activation maps from body-surface potentials via biophysically constrained and regularised optimisation [11], [18]. However, the inverse problem is severely ill-posed: distinct activation patterns can produce similar ECG observations, and small measurement noise can lead to large variations in the inferred solutions [18]. As a result, inverse ECG frameworks focus on electrical activity alone, without reconstructing cardiac geometry or mechanical motion [39].

Recent multimodal approaches attempt to combine ECG with cardiac imaging—such as CMR [17], CT [40], or electroanatomic mapping [19]—using latent alignment or regression-based models to improve physiological interpretability or predict localised properties (e.g., scar distribution [20] or activation patterns). Nevertheless, these methods still depend on explicit imaging input at inference [21] and remain

limited to task-specific, low-dimensional outputs [41]. Crucially, none of these approaches enable generative reconstruction of a complete 4D cardiac cine volume directly from ECG, nor do their representations support continuous cardiac motion or patient-specific anatomical variability required for organ-level CDTs [21]. This leaves a gap for ECG-driven organ-level reconstruction.

III. METHODOLOGY

A. Physiological Motion Modelling

To model physiologically plausible cardiac motion, we construct a topology-preserving volumetric registration framework that estimates a temporally coherent deformation field over the cardiac cycle.

Given two volumetric CMR fields acquired from the same subject at different cardiac phases,

$$V_s(\mathbf{x}), V_t(\mathbf{x}) : \Omega \subset \mathbb{R}^3 \rightarrow \mathbb{R}, \quad (1)$$

where $\mathbf{x} = (x, y, z)$ denotes spatial coordinates and $V(\mathbf{x})$ represents a volumetric CMR scalar field over the anatomical domain Ω , the objective is to estimate a displacement field $\mathbf{u}(\mathbf{x}) \in \mathbb{R}^3$ such that the source anatomy can be deformed toward the target configuration via a spatial transformation \mathcal{W} ,

$$\hat{V}_t(\mathbf{x}) = \mathcal{W}(V_s, \mathbf{u})(\mathbf{x}) = V_s(\mathbf{x} + \mathbf{u}(\mathbf{x})). \quad (2)$$

To ensure temporal smoothness and topology preservation across the cardiac cycle, the displacement field is parameterised as the time integration of a velocity field,

$$\mathbf{u}(\mathbf{x}) = \int_0^1 \mathbf{v}(\phi_t(\mathbf{x})) dt, \quad (3)$$

where ϕ_t denotes the deformation trajectory at pseudo-time $t \in [0, 1]$. This formulation enables the registration model to capture continuous cardiac motion as an underlying spatiotemporal deformation process.

The registration network is trained by minimising a composite objective that enforces both volumetric consistency and anatomical fidelity. Specifically, a reconstruction loss \mathcal{L}_{rec} based on normalised cross-correlation encourages consistency between V_t and \hat{V}_t . To further constrain the deformation to preserve clinically meaningful structures, we introduce a segmentation-guided teacher loss using a frozen nnU-Net [42] \mathcal{S}_ϕ . Both the target volume and the warped prediction are mapped back to the original CMR space and passed through \mathcal{S}_ϕ to obtain anatomical predictions for the left ventricle, right ventricle, and myocardium. The teacher predictions are converted to clean hard labels by retaining only the largest connected component of each structure, while the student branch preserves soft probabilities to enable gradient propagation. An anatomy-aware multi-class Dice loss is defined as

$$\mathcal{L}_{\text{seg}} = 1 - \frac{1}{C-1} \sum_{c=1}^{C-1} \frac{2 \sum_{\mathbf{x}} P_{\text{stud},c}(\mathbf{x}) Y_{\text{teach},c}(\mathbf{x})}{\sum_{\mathbf{x}} P_{\text{stud},c}^2(\mathbf{x}) + \sum_{\mathbf{x}} Y_{\text{teach},c}^2(\mathbf{x}) + \varepsilon}, \quad (4)$$

where C denotes the number of anatomical classes, $P_{\text{stud},c}$ and $Y_{\text{teach},c}$ represent the predicted soft probability and the

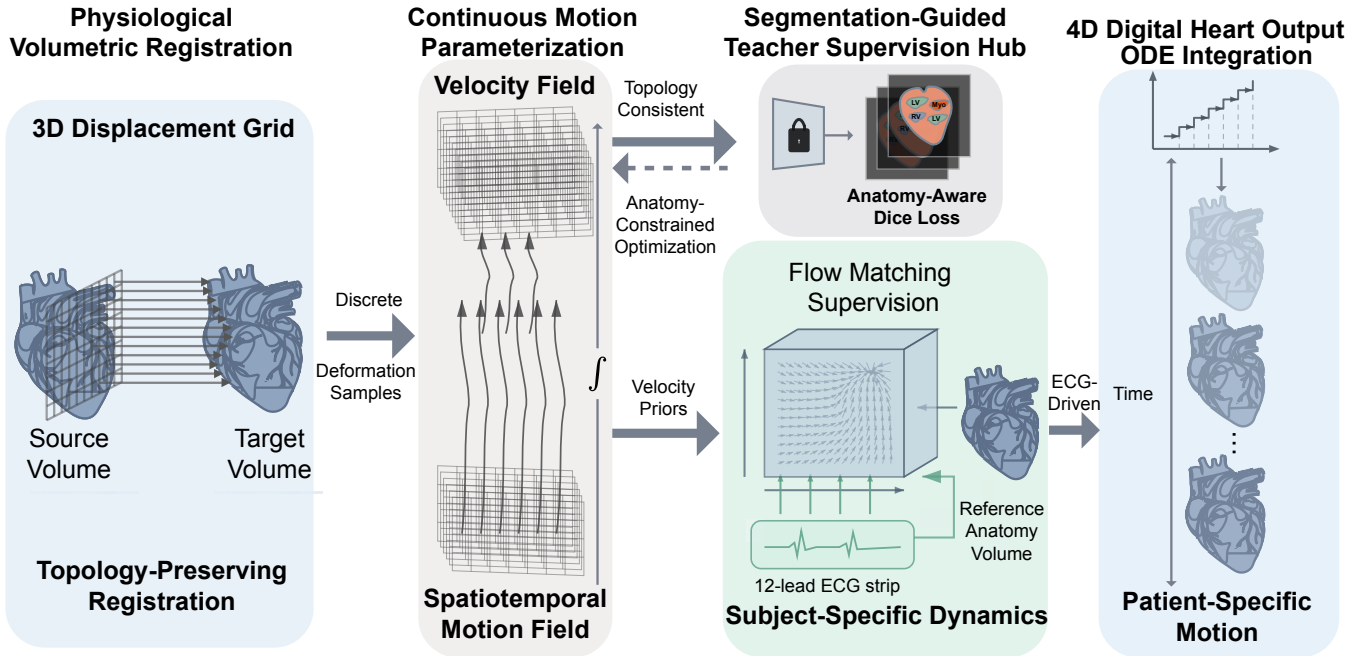


Fig. 2. Algorithmic pipeline of physiological motion modelling and ECG-conditioned digital heart construction. The pipeline starts with a topology-preserving volumetric registration module that estimates 3D displacement fields between source and target CMR volumes at different cardiac phases. Discrete deformation samples obtained from registration are parameterised as a continuous spatiotemporal velocity field. A segmentation-guided teacher supervision hub constrains the registration using anatomy-aware Dice loss. The resulting subject-specific motion dynamics are used as supervision for flow matching, linking ECG signals to physiological motion priors. Finally, the learned velocity field is integrated over time via ODE-based integration to produce a 4D digital heart with patient-specific cardiac motion.

corresponding one-hot teacher label for class c , respectively, and ε is a small constant for numerical stability.

The final optimisation objective of the physiological registration module is

$$\mathcal{L}_{\text{physio-reg}} = \lambda_{\text{rec}} \mathcal{L}_{\text{rec}} + \lambda_{\text{seg}} \mathcal{L}_{\text{seg}}, \quad (5)$$

which yields a mapping from pairs of cardiac phases to deformation fields that collectively parameterise cardiac motion over time,

$$f_{\theta} : (V_s, V_t) \mapsto \mathbf{u}. \quad (6)$$

Applying this registration sequentially across the cardiac cycle provides discrete samples of an underlying spatiotemporal deformation field,

$$\mathcal{U} = \{\mathbf{u}_1, \mathbf{u}_2, \dots, \mathbf{u}_T\}, \quad (7)$$

which serve as topology-consistent motion supervision for subsequent ECG-conditioned flow learning. The overall algorithmic pipeline is summarised in Fig. 2.

B. ECG-Conditioned Dynamic Flow Learning

Given the topology-consistent deformation fields from the registration stage, we learn an ECG-conditioned dynamic flow model that represents motion as a continuous velocity field over $\Omega \times [0, 1]$, enabling coherent 4D cardiac motion.

Specifically, we parameterise cardiac dynamics using a conditional velocity field

$$\mathbf{v}_{\theta} : \Omega \times [0, 1] \times \mathcal{C} \rightarrow \mathbb{R}^3, \quad \mathbf{v}_{\theta} = \mathbf{v}_{\theta}(\mathbf{x}, t, \mathbf{c}), \quad (8)$$

which models voxel-wise motion as a function of spatial location \mathbf{x} , continuous pseudo-time t , and subject-specific conditioning \mathbf{c} . The conditional embedding \mathbf{c} jointly encodes electrophysiological dynamics extracted from the ECG (\mathbf{c}_{ecg}) and anatomical context derived from the reference volume (\mathbf{c}_{rea}). In practice, \mathbf{c}_{ecg} is incorporated into the temporal embedding, while \mathbf{c}_{rea} is fused with intermediate feature representations to anchor the learned dynamics to subject-specific anatomy.

To supervise the learning of the spatiotemporal velocity field, we leverage the deformation trajectories estimated by the physiological registration module as motion priors. Specifically, a reference velocity field $\mathbf{v}^*(\mathbf{x}, t)$ is obtained from temporal derivatives of the registered deformation paths. The flow model is trained using a flow matching objective that aligns the predicted velocity field with these reference dynamics,

$$\mathcal{L}_{\text{FM}} = \mathbb{E}_{(\mathbf{x}, t) \sim \Omega \times [0, 1]} \left[\|\mathbf{v}_{\theta}(\mathbf{x}, t, \mathbf{c}) - \mathbf{v}^*(\mathbf{x}, t)\|_2^2 \right]. \quad (9)$$

By conditioning the velocity field on both ECG-derived temporal cues and reference-frame anatomy, the proposed model learns a continuous spatiotemporal flow that generates physiologically consistent and subject-specific cardiac motion, forming the core dynamic component of the 4D digital heart.

C. Patient-Specific Digital Heart Inference

At inference time, the learned ECG-conditioned spatiotemporal velocity field is integrated to generate subject-specific cardiac motion as a continuous deformation process over space

and time. Specifically, given the conditioning vector \mathbf{c} encoding ECG-derived dynamics and reference-frame anatomy, the velocity field \mathbf{v}_θ is numerically integrated using an ordinary differential equation (ODE) solver,

$$\hat{\mathcal{U}} = \text{ODESolve}(\mathbf{v}_\theta, \mathbf{c}), \quad (10)$$

yielding discrete samples of a continuous spatiotemporal deformation field over the cardiac cycle.

The resulting deformation fields $\hat{\mathcal{U}} = \{\hat{\mathbf{u}}_1, \dots, \hat{\mathbf{u}}_T\}$ are applied to the reference volumetric anatomy through the spatial transformation operator \mathcal{W} , producing a 4D cardiac volume defined over space and time,

$$\hat{\mathcal{J}}(\mathbf{x}, t) = \mathcal{W}(V_s, \hat{\mathbf{u}}(\mathbf{x}, t)) = V_s(\mathbf{x} + \hat{\mathbf{u}}(\mathbf{x}, t)), (\mathbf{x}, t) \in \Omega \times [0, 1]. \quad (11)$$

In practice, the continuous spatiotemporal volume $\hat{\mathcal{J}}(\mathbf{x}, t)$ is evaluated at T discrete cardiac phases, resulting in a temporally coherent 4D digital heart representation that preserves subject-specific anatomy while exhibiting physiologically plausible motion driven by the input ECG.

IV. EXPERIMENTS AND RESULTS

A. Set-up

1) *Datasets and preprocessing*: We evaluate our model on paired ECG and short-axis cine CMR data from the UK Biobank [43], comprising approximately 10,000 subjects after quality control. Each subject is represented by a single cardiac cycle reconstructed from 50 cine frames acquired using balanced steady-state free precession (bSSFP) imaging. Short-axis slices were stacked along the z -axis to form subject-level 3D+t cardiac volumes, which were resampled to a uniform spatial resolution and temporally aligned to a canonical cardiac cycle. For each subject, resting 12-lead ECG signals were extracted from XML-encoded UK Biobank records and converted to millivolts using acquisition metadata. All leads were synchronously sampled at 500 Hz. R-peaks were detected using NeuroKit2, and a representative R-R interval was selected to define a single-cycle electrical description of cardiac dynamics. The ECG segment between two adjacent R-peaks was cropped from all 12 leads and temporally aligned with the corresponding 4D cardiac volume. To obtain anatomical supervision at the organ level, 800 short-axis images were manually annotated under expert supervision and used to train a nnU-Net model. The trained network achieved a Dice score of 0.99 on a held-out test set and was subsequently applied to infer voxel-wise labels for all frames in each cine sequence, producing complete 4D segmentations of the left ventricle, right ventricle, and myocardium.

2) *Implementation details*: All models were implemented in PyTorch and trained on an NVIDIA A100 40G GPU. COF is optimised in a two-stage manner. In the first stage, the proposed TOPPR module is trained for 8,000 iterations using Adam with a learning rate of 1×10^{-4} and weight decay of 1×10^{-5} . In the second stage, the ECG-conditioned flow matching model is trained for another 8,000 iterations with the same optimiser settings. The batch size is set to 32, and gradient checkpointing is enabled to reduce memory

TABLE I
QUANTITATIVE COMPARISON OF ECG-CONDITIONED 4D DIGITAL HEART GENERATION ON THE UK BIOBANK DATASET.

| Method | SSIM \uparrow | PSNR \uparrow | FID \downarrow | FVD \downarrow | M-Corr. \uparrow | M-SSIM \uparrow |
|--------------------|-----------------|-----------------|------------------|------------------|--------------------|-------------------|
| COF | 0.984 | 28.46 | 6.39 | 17.60 | 0.474 | 0.894 |
| COF-w/ Diffusion | 0.976 | 27.45 | 8.74 | 31.45 | 0.297 | 0.878 |
| ECHOPulse [28] | 0.381 | 12.16 | 433.18 | 598.44 | 0.281 | 0.852 |
| LFDM [44] | 0.203 | 11.83 | 446.93 | 670.45 | 0.050 | 0.650 |
| EchoDiffusion [45] | 0.985 | 28.63 | 76.26 | 146.13 | 0.161 | 0.345 |
| Random Sample | 0.361 | 11.72 | 33.25 | 81.08 | 0.025 | 0.144 |

consumption. Fig. 3 visualises representative ECG-conditioned generation results and corresponding segmentation fidelity.

3) *Evaluation Metrics*: We comprehensively evaluate COF from anatomical fidelity, temporal coherence, cross-region robustness, and resolution generalisation, with a particular focus on organ-level consistency required for cardiac digital twin applications. **Image-level metrics**. We report SSIM, PSNR, Fréchet Inception Distance (FID), Fréchet Video Distance (FVD), Motion Correlation (M-Corr.), and Motion SSIM (M-SSIM). All metrics are computed on temporally coherent 3D+t volumes to reflect both spatial reconstruction quality and motion realism. Qualitative comparisons at key cardiac phases (ED/ES) are provided to illustrate anatomical sharpness and completeness of cardiac motion. **Region-aware anatomical evaluation**. To assess geometric fidelity across the full heart, each 3D volume is treated slice-wise. For each slice, Dice, IoU, and HD95 are computed by aggregating voxel-level errors over the entire region and across all cardiac phases. **Resolution-wise evaluation**. UK Biobank data exhibit substantial variability in in-plane spatial resolution (1.2 ~ 2.3 mm). For each subject, Dice, IoU, and HD95 are computed by aggregating voxel-wise errors over the full 4D cardiac cycle, yielding resolution-specific performance measurements at the organ level. **Digital-twin readiness**. We evaluate the suitability of COF for cardiac digital-twin applications by assessing organ-level functional and dynamical consistency across diverse disease categories. Functional indices—including EDV, ESV, EF, SV, and CO—are computed from the generated 4D cardiac masks. For each disease category, we compare predicted and CMR-derived measurements using MAE, RMSE, and Pearson/Spearman correlations, with correlation stability further examined via bootstrap resampling. Beyond scalar functional indices, we assess temporal fidelity by computing per-subject Pearson correlation between real and generated left ventricular volume–time curves.

B. ECG-conditioned 4D Digital Heart Reconstruction

We first evaluate reconstruction quality to verify fidelity and temporal coherence. Optical-flow–based baselines, including LFDM [44] and EchoDiffusion [45], depend on pseudo flow labels estimated in a separate stage; the resulting noisy and unreliable supervision leads to severe structural distortions or nearly motionless reconstructions, undermining organ-level fidelity. ECHOPulse [28] encodes anatomical appearance and ECG-driven dynamics within a single latent representation, causing errors in motion modelling to directly corrupt the static

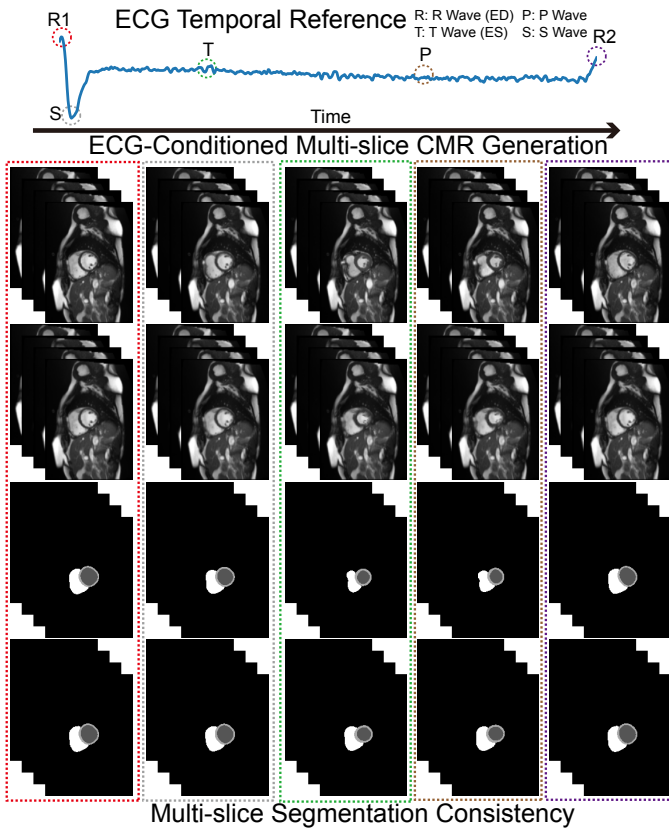


Fig. 3. ECG-conditioned digital heart generation results. A single R-R interval extracted from the 12-lead electrocardiogram is used as the temporal conditioning signal (top), where the R, S, T, and P waves indicate distinct cardiac phases. The R wave corresponds to the ED phase, while the T wave corresponds to the ES phase. On the left, the anatomical slice stack context is illustrated, showing the volumetric coverage of short-axis multi-slice CMR acquired across the heart. On the right, ECG-conditioned multi-slice CMR results are shown. For each selected cardiac phase, four rows are displayed: the first row shows the GT multi-slice CMR images, and the second row shows the corresponding ECG-conditioned generated slices. The third row presents the GT segmentation masks, while the fourth row shows the segmentation results obtained from the generated CMR slices.

cardiac anatomy. COF-w/ Diffusion replaces the final flow matching stage with diffusion-based sampling, whose conservative generation behaviour results in incomplete contraction at extreme phases of the cardiac cycle. In contrast, COF explicitly disentangles static anatomical structure from ECG-conditioned temporal dynamics and integrates them through a flow matching-based generative mechanism, enabling accurate reconstruction of continuous cardiac deformation while maintaining structural consistency across time. As summarised in Table I, COF achieves the best performance across all six quantitative metrics, establishing a new state of the art (Fig. 4). We further evaluate a downstream cardiac segmentation task. An nnU-Net model is applied to the generated sequences, and its predictions are compared against ground-truth 4D segmentation volumes for the left ventricle (LV), right ventricle (RV), and myocardium (Myo) on a per-frame basis. As reported in Table II, COF consistently yields higher Dice and IoU scores than all baselines across all cardiac structures, indicating that the reconstructed volumes retain

TABLE II
SEGMENTATION PERFORMANCE (Dice / IoU) ON GENERATED CMR SEQUENCES, EVALUATED USING A PRETRAINED nnU-NET.

| Method | LV | RV | Myo |
|--------------------|--------------------|--------------------|--------------------|
| COF | 0.87 / 0.80 | 0.74 / 0.61 | 0.85 / 0.74 |
| COF-w/ Diffusion | 0.83 / 0.75 | 0.66 / 0.52 | 0.81 / 0.71 |
| ECHOPulse [28] | 0.15 / 0.09 | 0.05 / 0.04 | 0.13 / 0.08 |
| LFDM [44] | 0.22 / 0.14 | 0.06 / 0.03 | 0.29 / 0.19 |
| EchoDiffusion [45] | 0.17 / 0.11 | 0.09 / 0.05 | 0.06 / 0.03 |
| Random Sample | 0.37 / 0.26 | 0.17 / 0.10 | 0.37 / 0.27 |

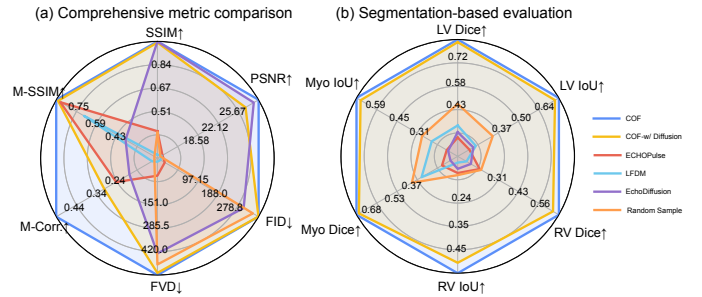


Fig. 4. (a) Radar-based comprehensive comparison across six image-level metrics (SSIM, PSNR, FID, FVD, M-Corr., and M-SSIM), where all indicators are normalised so that larger area indicates better overall performance. (b) Segmentation-based comparison using per-frame Dice and IoU for the left ventricle, right ventricle, and myocardium.

accurate anatomical boundaries and spatial relationships.

C. Cross-Modal Physiological Fusion

We perform a comprehensive ablation study to disentangle the respective roles of ECG-driven dynamics and anatomical anchoring. The results are summarised in Table III. Replacing the REA feature map with a zero tensor removes the static anatomical reference, leading to pronounced degradation in spatial consistency and organ shape preservation, as reflected by drops in SSIM. When the ECG embedding is incorrectly routed to the spatial branch, temporal dynamics become poorly modelled, resulting in increased FVD and reduced motion correlation, indicating weakened cycle-to-cycle physiological coherence. Removing the TOPPR causes the most severe performance collapse across all metrics, demonstrating that registration-guided flow supervision provides essential physiological constraints for learning realistic cardiac deformation trajectories. We further ablate the segmentation-consistency loss by varying its weighting factor λ_{seg} and by disabling the maximum-field constraint. Without segmentation consistency, the model produces anatomically unstable reconstructions, manifested by pronounced drops in Dice and IoU scores. Introducing segmentation supervision substantially improves anatomical fidelity across all cardiac structures, while moderate weighting ($\lambda_{\text{seg}} \in [0.5, 1.0]$) achieves the best trade-off between image quality, motion coherence, and segmentation accuracy. Excessively large weights yield diminishing returns, indicating that segmentation consistency primarily acts as a structural regulariser rather than a dominant optimisation objective.

TABLE III

ABLATION STUDY OF COF ON THE UK BIOBANK DATASET. UPPER BLOCK: MODULE-WISE ABLATIONS. LOWER BLOCK: SEGMENTATION-CONSISTENCY LOSS ABLATION.

| Configuration | Modules | | | Image metrics | | | | | | Segmentation metrics (Dice / IoU) | | |
|--|---------|-----|-------|-----------------|-----------------|------------------|------------------|--------------------|-------------------|-----------------------------------|--------------------|--------------------|
| | REA | ECG | TOPPR | SSIM \uparrow | PSNR \uparrow | FID \downarrow | FVD \downarrow | M-Corr. \uparrow | M-SSIM \uparrow | LV | RV | Myo |
| <i>Module ablations</i> | | | | | | | | | | | | |
| COF (no seg loss) | ✓ | ✓ | ✓ | 0.986 | 29.21 | 7.98 | 18.58 | 0.548 | 0.905 | | N/A | |
| w/o REA | × | ✓ | ✓ | 0.979 | 26.79 | 7.53 | 18.91 | 0.226 | 0.865 | | N/A | |
| w/o Temp. ECG | ✓ | × | ✓ | 0.978 | 26.76 | 14.50 | 25.24 | 0.512 | 0.896 | | N/A | |
| w/o TOPPR | ✓ | ✓ | × | 0.715 | 15.26 | 503.87 | 637.26 | 0.072 | 0.285 | | N/A | |
| <i>Segmentation-consistency loss ablation (COF variants)</i> | | | | | | | | | | | | |
| No max field | ✓ | ✓ | ✓ | 0.970 | 25.16 | 11.78 | 26.40 | 0.456 | 0.895 | 0.87 / 0.78 | 0.67 / 0.51 | 0.81 / 0.68 |
| $\lambda_{\text{seg}} = 0.5$ | ✓ | ✓ | ✓ | 0.982 | 27.94 | 7.34 | 17.74 | 0.533 | 0.901 | 0.88 / 0.80 | 0.71 / 0.58 | 0.84 / 0.74 |
| $\lambda_{\text{seg}} = 1.0$ | ✓ | ✓ | ✓ | 0.984 | 28.46 | 6.39 | 17.60 | 0.474 | 0.894 | 0.89 / 0.80 | 0.74 / 0.61 | 0.85 / 0.74 |
| $\lambda_{\text{seg}} = 3.0$ | ✓ | ✓ | ✓ | 0.975 | 26.04 | 12.28 | 28.43 | 0.498 | 0.901 | 0.85 / 0.76 | 0.64 / 0.50 | 0.83 / 0.71 |

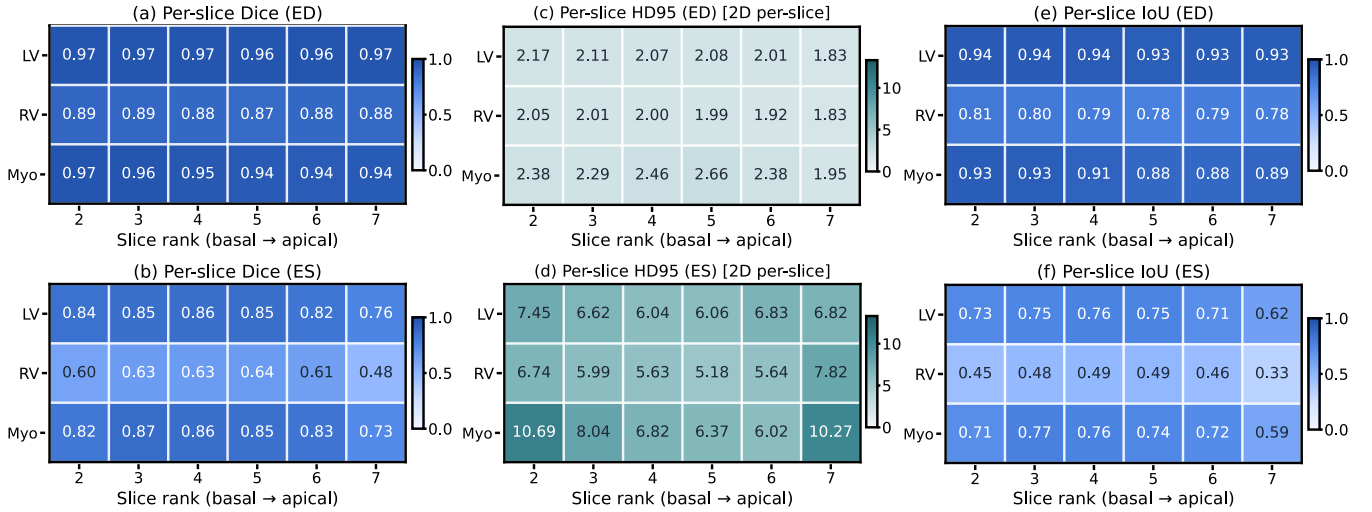


Fig. 5. Per-slice segmentation accuracy across cardiac phases. Per-slice Dice, HD95, and IoU are reported at the end-diastolic and end-systolic phases. Slices are ordered by slice rank from basal to apical (slice ranks 2–7). For each phase, metrics are computed separately for the left ventricle, right ventricle, and myocardium. Dice and IoU heatmaps (a, b, e, f) use a normalised scale from 0 to 1, while HD95 heatmaps (c, d) report 2D per-slice surface distances computed using in-plane spacing. Each cell represents the mean value across all subjects for the corresponding anatomical structure and slice rank.

D. Unified Multi-Slice, Multi-Resolution Representation

1) *Slice-wise analysis*: To test generalisation across slice positions, we conduct a slice-wise evaluation over the full short-axis stack of generated 4D volumes. For each subject, we evaluate two key cardiac phases—end-diastole (ED) and end-systole (ES)—and compute segmentation-based metrics between the generated and reference masks for the left ventricular cavity, right ventricular cavity, and myocardium. We adopt a data-driven anatomical grouping strategy based on myocardium coverage. We compute the myocardium area for each short-axis slice and identify the slice with maximal myocardium area as the anatomical centre. Slices with negligible myocardium presence are excluded by thresholding their area to at least 25% of the peak value. These slices are then ordered along the basal–apical axis and indexed by their relative slice rank. For each valid slice rank, structure, and phase (ED/ES), we compute Dice, IoU, and 95th-percentile Hausdorff distance (HD95). Dice and IoU are evaluated on a per-slice basis, while HD95 is computed in 2D using the original in-plane spatial resolution from the CMR header. Metrics are aggregated

across subjects to obtain mean performance profiles as a function of slice rank, which are visualised using slice-wise heatmaps for ED and ES (Fig. 5). COF maintains stable segmentation accuracy not only at mid–ventricular slices but also toward basal and apical regions, for both cavities and myocardium.

2) *Resolution-wise robustness*: To assess whether COF remains robust under heterogeneous acquisition resolutions, we conduct a resolution-wise analysis using the in-plane pixel spacing s_x extracted from the CMR header of each subject. For every case, we compare the generated 4D segmentation volume against the reference 4D labels (LV, RV, Myo) and compute Dice, IoU, and HD95. Concretely, for each subject we first compute *per-frame* metrics on the 3D volumes at all T timepoints and then average them over time to obtain subject-level scores. HD95 is computed on 3D surfaces using the original voxel spacing (s_x, s_y, s_z) . We additionally record the per-case s_x and retain all subject-level metrics for subsequent visualisation. We then partition the cohort into N_{bins} non-overlapping spacing intervals that uniformly cover the full

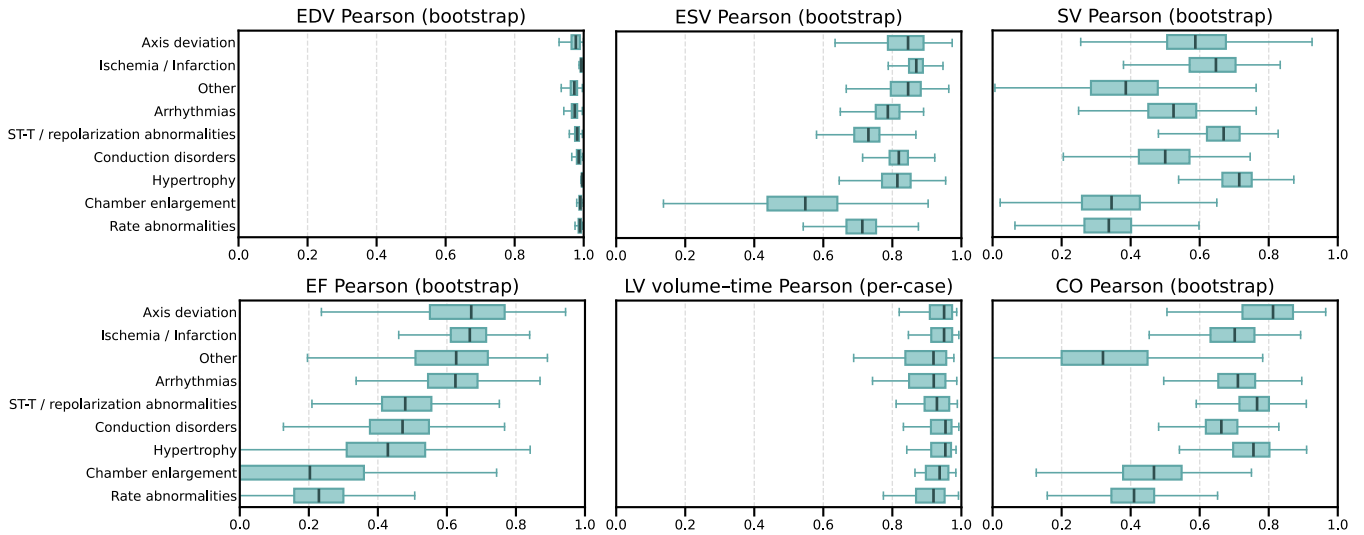


Fig. 6. Category-wise bootstrap distributions of functional agreement. Horizontal boxplots illustrate the distribution of Pearson correlation coefficients between generated and reference functional indices within each ECG diagnostic category. Panels report correlations for EDV, ESV, SV, EF, and CO estimated via bootstrap resampling (1,000 replicates per category), and the per-case Pearson correlation of LV volume-time curve.

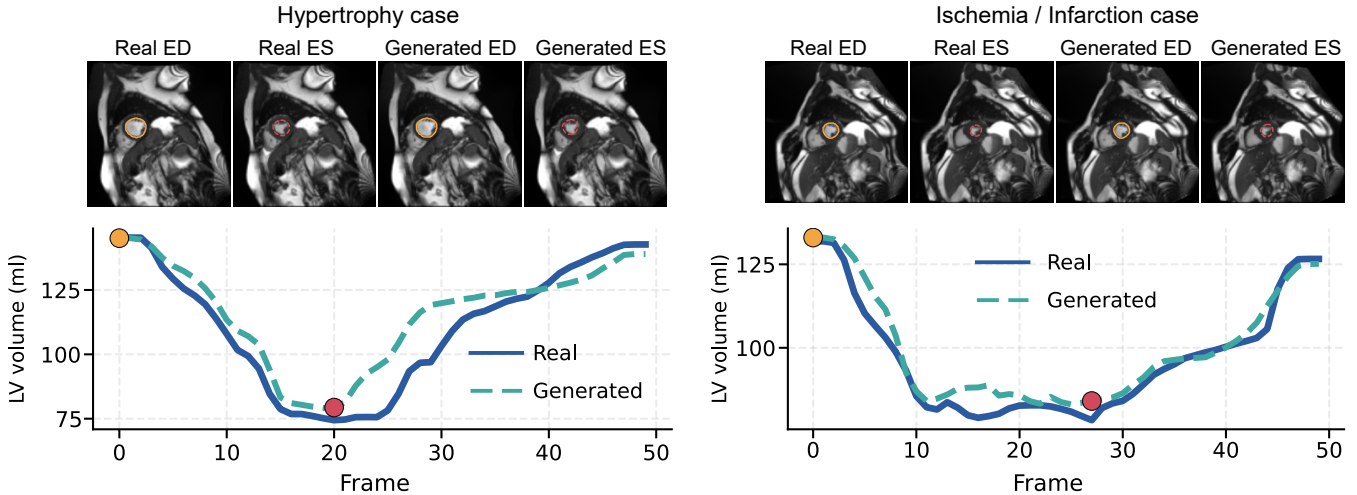


Fig. 7. Qualitative functional consistency in representative disease cases. Representative cases from hypertrophy and ischaemia/infarction groups are shown. For each case, the top row displays mid-ventricular short-axis CMR slices at end-diastole and end-systole, overlaid with left-ventricular contours from the real annotations and the generated results. The bottom row shows the corresponding LV volume-time curves: the real curve alone (left) and a comparison between real and generated curves (right). ED and ES frames are highlighted consistently in both the image contours and the volume-time plots.

range of observed s_x values. Within each bin, we aggregate the subject-level metrics for each structure and report the mean and standard deviation. These statistics are visualised using grouped bar plots with error bars. Beyond binned summaries, we further visualise resolution trends using per-case scatter plots of metric versus s_x together with structure-wise linear trend lines; the mean performance of each spacing bin is overlaid as larger markers (Fig. 8). Across the full spacing range, COF exhibits stable segmentation accuracy and no systematic performance degradation with increasing pixel spacing.

E. Digital-Twin-Oriented Functional Consistency

1) *Population-level consistency across ECG-derived disease categories*: We further evaluate whether COF preserves clinically meaningful 4D cardiac function across heterogeneous ECG-derived phenotypes. For each subject, we compute the

LV cavity volume at every timepoint from the 4D pseudo-segmentation labels (the same nnU-Net is applied to both real and generated cine volumes) and derive EDV, ESV, SV, and EF. We additionally estimate cardiac output (CO) by combining SV with the subject-specific heart rate. Subjects are grouped according to ECG-derived diagnostic categories, and agreement is quantified using Pearson correlations between real and generated measurements. To provide robust uncertainty estimates, we report bootstrap distributions of Pearson correlation for EDV/ESV/EF/SV/CO within each category. Fig. 6 summarises the category-wise correlation distributions for EDV, ESV, SV, EF, CO, and the full LV volume-time curve. Across major ECG categories, COF maintains stable correlations for both static functional indices and the entire contraction-relaxation trajectory, indicating that the ECG-to-4D digital heart reconstruction remains reliable under diverse

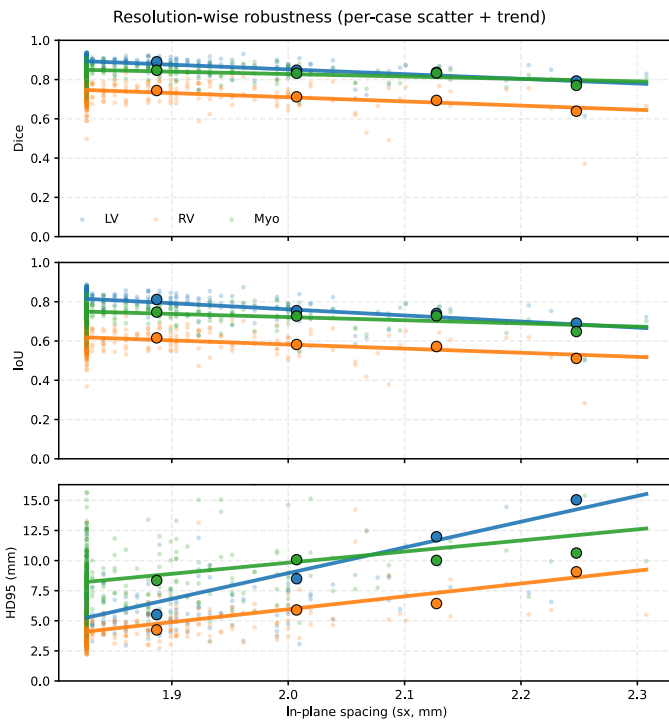


Fig. 8. Resolution-wise robustness analysis. Dice (top), IoU (middle), and HD95 (bottom) are plotted against the in-plane pixel spacing s_x (mm) for each case. Each point denotes one subject, with separate markers for LV, RV, and myocardium. Solid lines show linear trend fits over all cases for each structure. Large outlined markers indicate the mean metric value within each spacing bin.

rhythm, conduction, and repolarisation abnormalities.

2) *Case-level qualitative assessment in hypertrophic subjects*: To further demonstrate the suitability of COF for digital-heart reconstruction rather than image synthesis alone, we conduct a targeted case-level qualitative assessment on two representative ECG-derived disease categories with complementary pathophysiological characteristics: *Hypertrophy* and *Ischaemia / Infarction* (Fig. 7). These two conditions respectively emphasise structural remodelling and impaired contractile function. For the hypertrophic case, the generated end-diastolic and end-systolic contours accurately reproduce the enlarged LV cavity and the reduced systolic contraction typical of ventricular hypertrophy. The corresponding LV volume–time trajectory closely matches the reference curve in both amplitude and temporal evolution. In contrast, the ischaemia / infarction case is characterised by weakened systolic emptying and flattened volume dynamics. Despite these functional impairments, COF maintains accurate ED/ES geometry and reconstructs a physiologically plausible LV volume–time curve that aligns with the real trajectory across the entire cardiac cycle.

V. DISCUSSION AND CONCLUSION

In this study, we presented COF, a foundational ECG-conditioned generative framework for digital-heart reconstruction, enabling the synthesis of anatomically coherent and temporally continuous 4D cardiac states from a single cardiac cycle. COF is designed to recover patient-specific cardiac anatomy and dynamics as a unified, executable representation suitable for organ-level modelling.

The ability to reconstruct full 4D anatomy and motion directly from ECG signals marks a substantial shift from task-restricted predictive models toward generative, patient-specific virtual hearts. By preserving segmentation-meaningful geometry and physiologically interpretable deformation patterns, COF establishes a structural foundation that supports simulation, volumetric quantification, regional functional assessment, and disease-specific modelling. This organ-level reconstruction capability is particularly valuable for clinical cardiac digitization technologies, enabling continuous patient monitoring and longitudinal cardiac modelling in settings where CMR is unavailable but ECG is widely accessible.

Despite its strong performance, COF has several limitations that point toward important future directions. First, the current framework relies on R–R–interval–based ECG preprocessing and does not explicitly model beat-to-beat variability, arrhythmic cycles, or multi-cycle temporal dependencies. Extending the model to operate on continuous ECG streams may substantially improve robustness in patients with rhythm irregularities and enable long-term cardiac state tracking. Second, although COF effectively integrates dynamic information, the reconstruction process fundamentally depends on a static anatomical anchor frame. Without this anchor, the model cannot reliably infer subject-specific geometry. Future work may explore generative mechanisms that jointly infer anatomy and motion without requiring explicit anchor-frame supervision, potentially enabling purely electrophysiology-driven virtual heart reconstruction.

REFERENCES

- [1] G. A. Roth, G. A. Mensah, C. O. Johnson, G. Addolorato, E. Ammirati, L. M. Baddour, N. C. Barengo, A. Z. Beaton, E. J. Benjamin, C. P. Benziger *et al.*, “Global burden of cardiovascular diseases and risk factors, 1990–2019: update from the gbd 2019 study,” *Journal of the American college of cardiology*, vol. 76, no. 25, pp. 2982–3021, 2020.
- [2] C. M. Kramer, J. Barkhausen, S. D. Flamm, R. J. Kim, and E. Nagel, “Standardized cardiovascular magnetic resonance imaging (cmr) protocols, society for cardiovascular magnetic resonance: board of trustees task force on standardized protocols,” *Journal of Cardiovascular Magnetic Resonance*, vol. 10, no. 1, p. 35, 2008.
- [3] E. Potter and T. H. Marwick, “Assessment of left ventricular function by echocardiography: the case for routinely adding global longitudinal strain to ejection fraction,” *JACC: Cardiovascular Imaging*, vol. 11, no. 2 Part 1, pp. 260–274, 2018.
- [4] A. H. A. W. G. on Myocardial Segmentation, R. for Cardiac Imaging:, M. D. Cerqueira, N. J. Weissman, V. Dilsizian, A. K. Jacobs, S. Kaul, W. K. Laskey, D. J. Pennell, J. A. Rumberger, T. Ryan *et al.*, “Standardized myocardial segmentation and nomenclature for tomographic imaging of the heart: a statement for healthcare professionals from the cardiac imaging committee of the council on clinical cardiology of the american heart association,” *Circulation*, vol. 105, no. 4, pp. 539–542, 2002.
- [5] G. Coorey, G. A. Figtree, D. F. Fletcher, V. J. Snelson, S. T. Vernon, D. Winlaw, S. M. Grieve, A. McEwan, J. Y. H. Yang, P. Qian *et al.*, “The health digital twin to tackle cardiovascular disease—a review of an emerging interdisciplinary field,” *NPJ digital medicine*, vol. 5, no. 1, p. 126, 2022.
- [6] J. Corral-Acero, F. Margara, M. Marciniak, C. Rodero, F. Loncaric, Y. Feng, A. Gilbert, J. F. Fernandes, H. A. Bukhari, A. Wajdan *et al.*, “The ‘digital twin’ to enable the vision of precision cardiology,” *European heart journal*, vol. 41, no. 48, pp. 4556–4564, 2020.
- [7] R. A. Gray and P. Pathmanathan, “Patient-specific cardiovascular computational modeling: diversity of personalization and challenges,” *Journal of cardiovascular translational research*, vol. 11, no. 2, pp. 80–88, 2018.

- [8] S. E. Petersen, N. Aung, M. M. Sanghvi, F. Zemrak, K. Fung, J. M. Paiva, J. M. Francis, M. Y. Khanji, E. Lukaschuk, A. M. Lee *et al.*, "Reference ranges for cardiac structure and function using cardiovascular magnetic resonance (cmr) in caucasians from the uk biobank population cohort," *Journal of cardiovascular magnetic resonance*, vol. 19, no. 1, p. 18, 2016.
- [9] T. Betemariam, A. Aleka, E. Ahmed, T. Worku, Y. Mebrahtu, E. Androulakis, S. E. Petersen, and R. Friebe, "Barriers to cardiovascular magnetic resonance imaging scan performance and reporting by cardiologists: a systematic literature review," *European Heart Journal-Imaging Methods and Practice*, vol. 3, no. 1, p. qyaf010, 2025.
- [10] Z. I. Attia, P. A. Noseworthy, F. Lopez-Jimenez, S. J. Asirvatham, A. J. Deshmukh, B. J. Gersh, R. E. Carter, X. Yao, A. A. Rabinstein, B. J. Erickson *et al.*, "An artificial intelligence-enabled ecg algorithm for the identification of patients with atrial fibrillation during sinus rhythm: a retrospective analysis of outcome prediction," *The Lancet*, vol. 394, no. 10201, pp. 861–867, 2019.
- [11] Y. Rudy and J. E. Burnes, "Noninvasive electrocardiographic imaging," *Annals of Noninvasive Electrocardiology*, vol. 4, no. 3, pp. 340–359, 1999.
- [12] H. S. Oster, B. Taccardi, R. L. Lux, P. R. Ershler, and Y. Rudy, "Noninvasive electrocardiographic imaging: reconstruction of epicardial potentials, electrograms, and isochrones and localization of single and multiple electrocardiac events," *Circulation*, vol. 96, no. 3, pp. 1012–1024, 1997.
- [13] N. G. Bellenger, M. I. Burgess, S. G. Ray, A. Lahiri, A. J. Coats, J. G. Cleland, and D. J. Pennell, "Comparison of left ventricular ejection fraction and volumes in heart failure by echocardiography, radionuclide ventriculography and cardiovascular magnetic resonance. are they interchangeable?" *European heart journal*, vol. 21, no. 16, pp. 1387–1396, 2000.
- [14] R. M. Lang, L. P. Badano, V. Mor-Avi, J. Afilalo, A. Armstrong, L. Ernande, F. A. Flachskampf, E. Foster, S. A. Goldstein, T. Kuznetsova *et al.*, "Recommendations for cardiac chamber quantification by echocardiography in adults: an update from the american society of echocardiography and the european association of cardiovascular imaging," *European Heart Journal-Cardiovascular Imaging*, vol. 16, no. 3, pp. 233–271, 2015.
- [15] N. A. Trayanova, "Computational cardiology: the heart of the matter," *International Scholarly Research Notices*, vol. 2012, no. 1, p. 269680, 2012.
- [16] S. Somani, A. J. Russak, F. Richter, S. Zhao, A. Vaid, F. Chaudhry, J. K. De Freitas, N. Naik, R. Miotto, G. N. Nadkarni *et al.*, "Deep learning and the electrocardiogram: review of the current state-of-the-art," *EP Europace*, vol. 23, no. 8, pp. 1179–1191, 2021.
- [17] B. F. Nielsen, M. Lysaker, and P. Grøttum, "Computing ischemic regions in the heart with the bidomain model—first steps towards validation," *IEEE Transactions on Medical Imaging*, vol. 32, no. 6, pp. 1085–1096, 2013.
- [18] R. S. MacLeod and D. H. Brooks, "Recent progress in inverse problems in electrocardiology," *IEEE Engineering in Medicine and Biology Magazine*, vol. 17, no. 1, pp. 73–83, 1998.
- [19] J. Dhamala, P. Bajracharya, H. J. Arevalo, J. L. Sapp, B. M. Horáček, K. C. Wu, N. A. Trayanova, and L. Wang, "Embedding high-dimensional bayesian optimization via generative modeling: parameter personalization of cardiac electrophysiological models," *Medical image analysis*, vol. 62, p. 101670, 2020.
- [20] L. Li, J. Camps, Z. J. Wang, M. Beetz, A. Banerjee, B. Rodriguez, and V. Grau, "Toward enabling cardiac digital twins of myocardial infarction using deep computational models for inverse inference," *IEEE transactions on medical imaging*, vol. 43, no. 7, pp. 2466–2478, 2024.
- [21] L. Li, J. Camps, B. Rodriguez, and V. Grau, "Solving the inverse problem of electrocardiography for cardiac digital twins: A survey," *IEEE Reviews in Biomedical Engineering*, 2024.
- [22] J. Xie and B. Yao, "Physics-constrained deep learning for robust inverse ecg modeling," *IEEE Transactions on Automation Science and Engineering*, vol. 20, no. 1, pp. 151–166, 2022.
- [23] A. Chartsias, T. Joyce, G. Papanastasiou, S. Semple, M. Williams, D. Newby, R. Dharmakumar, and S. A. Tsafaris, "Factorised spatial representation learning: Application in semi-supervised myocardial segmentation," in *International Conference on Medical Image Computing and Computer-Assisted Intervention*. Springer, 2018, pp. 490–498.
- [24] X. Yi, E. Walia, and P. Babyn, "Generative adversarial network in medical imaging: A review," *Medical image analysis*, vol. 58, p. 101552, 2019.
- [25] Q. Meng, W. Bai, D. P. O'Regan, and D. Rueckert, "Deepmesh: Mesh-based cardiac motion tracking using deep learning," *IEEE transactions on medical imaging*, vol. 43, no. 4, pp. 1489–1500, 2023.
- [26] C. Qin, W. Bai, J. Schlemper, S. E. Petersen, S. K. Piechnik, S. Neubauer, and D. Rueckert, "Joint learning of motion estimation and segmentation for cardiac mr image sequences," in *International Conference on Medical Image Computing and Computer-Assisted Intervention*. Springer, 2018, pp. 472–480.
- [27] Y. Blau and T. Michaeli, "The perception-distortion tradeoff," in *Proceedings of the IEEE conference on computer vision and pattern recognition*, 2018, pp. 6228–6237.
- [28] Y. Li, S. Kim, Z. Wu, H. Jiang, Y. Pan, P. Jin, S. Song, Y. Shi, T. Liu, Q. Li *et al.*, "Echopulse: Ecg controlled echocardiograms video generation," *arXiv preprint arXiv:2410.03143*, 2024.
- [29] N. Cheng, "Deep generative model for synthesising and analysing cardiac magnetic resonance images," Ph.D. dissertation, University of Leeds, 2025.
- [30] S. Ahn, W. Park, and J. Park, "Are medical image generative models biologically trustworthy?" in *Proceedings of the IEEE/CVF International Conference on Computer Vision*, 2025, pp. 633–643.
- [31] X. Fang, Z. Ding, J. Cai, Y. Xiao, B. Liu, J. Jin, H. Wang, G. Nie, S. Huang, T. Chen *et al.*, "Ecgflowcmr: Pretraining with ecg-generated cine cmr improves cardiac disease classification and phenotype prediction," *arXiv preprint arXiv:2601.20904*, 2026.
- [32] S. Hong, Y. Zhou, J. Shang, C. Xiao, and J. Sun, "Opportunities and challenges of deep learning methods for electrocardiogram data: A systematic review," *Computers in biology and medicine*, vol. 122, p. 103801, 2020.
- [33] Z. I. Attia, S. Kapa, X. Yao, F. Lopez-Jimenez, T. L. Mohan, P. A. Pellikka, R. E. Carter, N. D. Shah, P. A. Friedman, and P. A. Noseworthy, "Prospective validation of a deep learning electrocardiogram algorithm for the detection of left ventricular systolic dysfunction," *Journal of cardiovascular electrophysiology*, vol. 30, no. 5, pp. 668–674, 2019.
- [34] A. Y. Hannun, P. Rajpurkar, M. Haghpanahi, G. H. Tison, C. Bourn, M. P. Turakhia, and A. Y. Ng, "Cardiologist-level arrhythmia detection and classification in ambulatory electrocardiograms using a deep neural network," *Nature medicine*, vol. 25, no. 1, pp. 65–69, 2019.
- [35] Y. Ansari, O. Mourad, K. Qaraqe, and E. Serpedin, "Deep learning for ecg arrhythmia detection and classification: an overview of progress for period 2017–2023," *Frontiers in Physiology*, vol. 14, p. 1246746, 2023.
- [36] D. J. Engelen, A. P. Gorgels, E. C. Cheriex, E. D. De Muinck, A. J. Oude Ophuis, W. R. Dassen, J. Vainer, V. G. van Ommen, and H. J. Wellens, "Value of the electrocardiogram in localizing the occlusion site in the left anterior descending coronary artery in acute anterior myocardial infarction," *Journal of the American College of Cardiology*, vol. 34, no. 2, pp. 389–395, 1999.
- [37] H. Akbar and S. Mountfort, "Acute st-segment elevation myocardial infarction (stemi)," *StatPearls*, 2024.
- [38] R. H. Selvester, G. S. Wagner, and N. B. Hindman, "The selvester qrs scoring system for estimating myocardial infarct size: the development and application of the system," *Archives of Internal Medicine*, vol. 145, no. 10, pp. 1877–1881, 1985.
- [39] H. Pereira, S. Niederer, and C. A. Rinaldi, "Electrocardiographic imaging for cardiac arrhythmias and resynchronization therapy," 2020.
- [40] C. Ramanathan, R. N. Ghanem, P. Jia, K. Ryu, and Y. Rudy, "Noninvasive electrocardiographic imaging for cardiac electrophysiology and arrhythmia," *Nature medicine*, vol. 10, no. 4, pp. 422–428, 2004.
- [41] H. J. Arevalo, F. Vadakkumpadan, E. Guallar, A. Jebb, P. Malamas, K. C. Wu, and N. A. Trayanova, "Arrhythmia risk stratification of patients after myocardial infarction using personalized heart models," *Nature communications*, vol. 7, no. 1, p. 11437, 2016.
- [42] F. Isensee, P. F. Jaeger, S. A. Kohl, J. Petersen, and K. H. Maier-Hein, "nnu-net: a self-configuring method for deep learning-based biomedical image segmentation," *Nature methods*, vol. 18, no. 2, pp. 203–211, 2021.
- [43] S. E. Petersen, P. M. Matthews, J. M. Francis, M. D. Robson, F. Zemrak, R. Boubertakh, A. A. Young, S. Hudson, P. Weale, S. Garratt *et al.*, "Uk biobank's cardiovascular magnetic resonance protocol," *Journal of cardiovascular magnetic resonance*, vol. 18, no. 1, p. 8, 2016.
- [44] H. Ni, B. Egger, S. Lohit, A. Cherian, Y. Wang, T. Koike-Akino, S. X. Huang, and T. K. Marks, "Ti2v-zero: Zero-shot image conditioning for text-to-video diffusion models," in *Proceedings of the IEEE/CVF conference on computer vision and pattern recognition*, 2024, pp. 9015–9025.
- [45] H. Reynaud, M. Qiao, M. Dombrowski, T. Day, R. Razavi, A. Gomez, P. Leeson, and B. Kainz, "Feature-conditioned cascaded video diffusion models for precise echocardiogram synthesis," in *International Conference on Medical Image Computing and Computer-Assisted Intervention*. Springer, 2023, pp. 142–152.